Preparation and Characterization of All-biomass Histidine/Regenerated Cellulose Composite Nanospheres

Jing Chen,[b,†] Jundong Shi,[b,†] Yihan Sun,[b] Ke Jiang,[b] Xin Huang,[a] Xiaoying Ji,[a] Ying Liu,[a] Jian Zhou,[a,*] Yanju Liu,[a,*] Yaxi Liu,[c,*] and Shaobo Zhang [b,*]

The unique imidazole group of histidine endows materials containing it with pH responsiveness, metal-coordination capability, and π–π stacking interactions. However, the development of fully bio-based nanostructured supports that enable efficient histidine immobilization while maintaining abundant accessible surface functional groups remains largely unexplored. In this study, regenerated cellulose nanospheres (RCNs) with an average particle size of 88.8 ± 2.1 nm were prepared through a dissolution–regeneration process and subsequently oxidized to introduce reactive aldehyde groups. Histidine was then covalently grafted onto the RCN surface *via* a Schiff base reaction, yielding fully bio-based histidine/regenerated cellulose composite nanospheres (His-RCNs) with an average particle size of 39.3 ± 1.1 nm. The reduced particle size after grafting is expected to provide greater accessible surface area for interfacial interactions and subsequent functionalization. Morphological, structural, and thermal analyses confirmed the successful grafting of histidine while preserving the regenerated cellulose framework and spherical morphology. Quantitative analysis revealed that regenerated cellulose and grafted histidine accounted for 79.2 wt% and 20.8 wt% of the final product, respectively. By integrating the renewable regenerated cellulose nanosphere platform with multifunctional imidazole groups, this work provides a fully bio-based strategy for constructing histidine-functionalized cellulose nanomaterials.

DOI: 10.15376/biores.21.4.9747-9760

Keywords: Regenerated cellulose; Nanospheres; Histidine; Biomass

*Contact information: a: China Tobacco Sichuan Industrial Co., Ltd., Harmful Components and Tar Reduction in Cigarette Key Laboratory of Sichuan Province, Chengdu 610017, China; b: Forest Ecology and Conservation in the Upper Reaches of the Yangtze River Key Laboratory of Sichuan Province, College of Forestry, Sichuan Agricultural University, Chengdu 611130, China; c: State Key Laboratory of Crop Gene Exploration and Utilization in Southwest China, Sichuan Agricultural University, Chengdu 611130, China; †: These authors contributed equally to this work; *Corresponding authors: zhoujian8860@163.com; 524112919@qq.com; liuyaxi@sicau.edu.cn; shaobo_z@sicau.edu.cn*

INTRODUCTION

Histidine, one of the naturally occurring essential amino acids, serves as a ligand for transition metal ions and as an important carrier in proton transfer processes, thereby playing diverse roles in various biological systems (Chen *et al.* 2022). As a naturally occurring amino acid, L-histidine is widely distributed in protein-rich biomass, with contents of approximately 2.3 to 3.2 g per 100 g protein in common cereals such as wheat, rye, and barley (Rani *et al*. 2021). It can be obtained from biomass-derived proteins through

protein hydrolysis or produced from renewable biomass feedstocks *via* microbial fermentation (Kim *et al.* 2024). Compared with other amino acids, histidine has a unique imidazole-containing side chain, which provides reversible protonation/deprotonation behavior and endows it with multifunctional interaction capabilities. The imidazole group can act as a σ-donor and π-acceptor ligand, enabling histidine to establish coordination interactions with various metal ions, as well as π–π stacking and hydrogen-bonding interactions with aromatic or functional molecules (Sigel 1971; Kramer 1996). Because of the unique characteristics of the imidazole ring, including pH responsiveness, hydrogen-bonding capability, and excellent coordination and stacking interactions, histidine has demonstrated significant advantages in interfacial materials, self-assembly of nanomaterials (Anderson *et al.* 2010; Hsu *et al.* 2024; Meena *et al.* 2024), and adsorption materials (Dehghani *et al.* 2021; Tian *et al.* 2024).

Leveraging these unique physicochemical properties, histidine functionalization has emerged as an effective strategy for introducing metal-coordination, hydrogen-bonding, and self-assembly capabilities into various material platforms, leading to promising applications in biomedicine, nanotechnology, coatings, and related fields (Chung *et al.* 2011; Levin *et al.* 2020; Dehghani *et al.* 2021). For example, Jia *et al.* synthesized an integrated intelligent inhibitor nanocontainer assembled from L-histidine, halloysite nanotubes, and reduced graphene oxide. This material exhibits excellent compatibility with waterborne coatings and provides multifunctional anticorrosion protection when used as a modifier in waterborne coating systems (Jia *et al.* 2020). Similarly, Yang *et al*. developed a nanomedicine strategy by combining surface roughness-controlled ceria nanocages with poly(L-histidine) surface coatings (Yang *et al*. 2023). This design endowed the nanocarriers with multiple bioactive functions, promoted transport across corneal epithelial barriers, and enabled the on-demand release of acetylcholine chloride and SB431542 at the lesion site. In another study, Zhang *et al.* reported the systematic design of a histidine-rich lipidated peptide sequence, in which histidine and stearic acid initially interact with the graphite surface through π–π stacking and hydrophobic interactions. Subsequently, peptide molecules undergo surface-assisted assembly *via* hydrogen bonding between deprotonated histidine segments, forming a textured peptide nanostructure. This strategy enables the simultaneous exfoliation of graphite flakes and functionalization of the resulting graphene nanosheets, providing long-term dispersion stability in aqueous solution (Zhang *et al.* 2019). These studies highlight the versatility of histidine as a multifunctional molecular component for constructing advanced functional materials, while also emphasizing the importance of developing renewable nanostructured platforms that can effectively integrate histidine functionalities.

Cellulose-based nanomaterials, derived from cellulose—the most abundant renewable polysaccharide on Earth (Moon *et al.* 2011; Li *et al.* 2021)—have attracted considerable attention owing to their renewable nature, nanoscale dimensions, excellent mechanical properties, abundant surface hydroxyl groups, and versatile surface chemistry (Das *et al.* 2022; Österberg *et al.* 2023). Recently, due to the outstanding properties of nanocellulose, it has been increasingly recognized for its innovative applications in many advanced fields, including electronics, energy generation, and the automotive sector (Shojaeiarani *et al.* 2021; Mhlongo *et al.* 2022; Pradhan *et al.* 2022). The abundant surface hydroxyl groups, nanoscale dimensions, and renewable nature of nanocellulose make it an ideal scaffold for introducing functional biomolecules. Previous studies have demonstrated that amino acids can be covalently integrated with oxidized nanocellulose through amide coupling, while amino acid-functionalized nanocellulose materials have also been

developed for metal-ion adsorption applications (Barazzouk and Daneault 2011; Yuan *et al*. 2025). Generally, nanocellulose materials are mainly categorized into rod-like cellulose nanocrystals (CNC) and fibrous cellulose nanofibers (CNF) based on their morphologies (Österberg *et al.* 2023). However, their anisotropic structures tend to promote particle entanglement and aggregation, thereby reducing the accessibility of surface functional groups and limiting the efficiency of subsequent functionalization. Therefore, cellulose-based nanomaterials with alternative morphologies are desirable for improving surface functionalization efficiency. Regenerated cellulose nanospheres (RCNs) represent a recently developed class of cellulose-based nanomaterials with a spherical morphology, attracting increasing interest because of their distinctive structural characteristics and application potential (Yupanqui-Mendoza and Arantes 2024). Compared with conventional rod-like CNCs and fibrous CNFs, the isotropic spherical morphology of RCNs reduces particle entanglement and facilitates more homogeneous surface functionalization, while also contributing to improved suspension stability and particle packing (Zheng *et al.* 2019; Tian *et al*. 2022). These characteristics have enabled various applications, such as reinforcing polymer composites and improving coating adhesion (Li *et al.* 2015 and Li *et al*. 2025). Consequently, RCNs have emerged as attractive platforms for constructing functional bio-based nanomaterials, including nanocomposite additives and other bio-based functional systems (Rampazzo *et al*. 2017; Cui *et al.* 2018; Lu *et al*. 2016).

In this study, cellulose—the main structural component of plants—was used as the raw material to prepare RCNs through a dissolution–regeneration process. Using RCNs as the matrix, fully bio-based histidine/ regenerated cellulose composite nanospheres (His-RCNs) were subsequently fabricated. Specifically, RCNs was first pretreated with sodium periodate to introduce highly reactive aldehyde groups on its surface. Subsequently, the amino groups of histidine were condensed with the aldehyde groups of RCNs *via* a Schiff base reaction, resulting in the formation of His-RCNs.

EXPERIMENTAL

Materials

Cellulose (technical grade) was purchased from Sangon Biotech (Shanghai) Co., Ltd. Sodium hydroxide (NaOH, AR), urea (AR), and thiourea (AR) were obtained from Sinopharm Chemical Reagent Co., Ltd. Glacial acetic acid (AR) and ethylene glycol (AR) were procured from Chengdu Kelong Chemical Co., Ltd. Phosphate-buffered saline (PBS, 0.02 mol/L, pH 7.4) was acquired from Chengdu NanoNovel Information Technology Co., Ltd., while L-Histidine (His, AR) was sourced from Shandong Keyuan Biochemical Co., Ltd. Sodium periodate ($NaIO_4$, AR) was obtained from Chengdu Jinshan Chemical Reagent Co., Ltd.

Preparation of RCNs

Briefly, an aqueous solution containing sodium hydroxide (8 wt%), urea (8 wt%), and thiourea (6.5 wt%) was precooled to −10 °C. Subsequently, 1.5 g of cellulose was dispersed into the solution and stirred at −10 °C for 30 to 40 min at a rotational speed of 2000 r/min until the cellulose was completely dissolved. The resulting solution was then centrifuged at 11000 r/min for 20 min to remove the insoluble fraction, yielding a transparent and clear cellulose solution. The supernatant was slowly poured into 2000 mL

of deionized water and stirred at a speed lower than 60 rpm for 30 min to regenerate RCNs. The suspension was washed with deionized water until the pH reached 7. The resulting white suspension was further subjected to ultrasonication at a power of 600 W for 30 min to obtain a stable RCNs dispersion.

Preparation of Dialdehyde RCNs

$NaIO_4$ was added to the stirred RCNs dispersion with a mass ratio of RCNs to $NaIO_4$ of 1:2 (Sun *et al.* 2015). The pH of the system was then adjusted to 4.5 using dilute acetic acid. Subsequently, the mixture was stirred and reacted at 40 °C for 4 h. During the reaction, the system was completely covered with aluminum foil to avoid the photodecomposition of $NaIO_4$ (Ram *et al.* 2018). After 4 h, 10 mL of ethylene glycol was added to terminate the reaction. The precipitate was collected by centrifugation and washed repeatedly with deionized water by centrifugation until neutral. The obtained product was then dried in an oven at 60 °C to obtain dialdehyde RCNs (DA-RCNs).

Preparation of His-RCNs

DA-RCNs and His with a mass ratio of 1:2 were dispersed in 100 mL of PBS solution (pH = 7.4). The mixture was stirred and allowed to react at 25 °C for 48 h. After the reaction, the precipitate was collected by centrifugation and washed repeatedly with deionized water by centrifugation until neutral. The obtained product was then dried in an oven at 60 °C to yield brownish-yellow His-RCNs.

Fourier Transform Infrared (FTIR) Spectroscopy

The FTIR spectroscopy (Nicolet IS5, Thermo Fisher Scientific, USA) was used to qualitatively analyze the functional groups in cellulose, RCNs, DA-RCNs, His, and His-RCNs. Each sample was scanned 32 times in the range of 400 to 4000 cm^{-1} with a resolution of 4 cm^{-1}.

Scanning Electron Microscopy (SEM)

The microscopic morphology of RCNs and His-RCNs was characterized using SEM (Gemini 300, ZEISS, Germany) at an accelerating voltage of 2.00 kV. Droplets of RCNs and His-RCNs suspensions were deposited onto a silicon wafer and dried, followed by platinum sputter-coating to improve electrical conductivity. Approximately 100 particles in each SEM image were measured using ImageJ software to calculate the average diameters of RCNs and His-RCNs.

Thermogravimetric Analysis (TGA)

The thermogravimetric behavior of His, RCNs, and His-RCNs was analyzed using a SDT 650 thermogravimetric analyzer (TA Instruments, New Castle, DE, USA) under a nitrogen atmosphere. The temperature range was from 0 to 800 °C with a heating rate of 10 °C/min.

To quantitatively estimate the component ratio in His-RCNs, the high-temperature residue obtained from the TGA curves was used. It was assumed that the residue of the grafted product was the mass-weighted average of the residues of each component and that no obvious thermal interaction occurred between the components. The mass residues at 800 °C (the final temperature at which organic components were completely decomposed under the experimental conditions) were obtained from the TGA curves: R_{RCNs} for RCNs, R_{His} for His, and R_{Graft} for His-RCNs. The mass fraction of RCNs in the grafted product is

denoted as x, and the mass fraction of His is denoted as y, which satisfy the following relationship:

$$x + y = 1 \quad (1)$$

$$x \cdot R_{RCNs} + y \cdot R_{His} = R_{graft}$$

Determination of Imidazole Ring Content in His-RCNs

The imidazole ring content in the samples was determined by an acid–base titration method (Kovaleva *et al.* 2008). Briefly, 0.1 g of dried His-RCNs was mixed with 50 mL of 0.1 mol/L hydrochloric acid in a flask and refluxed in a water bath at 100 °C for 1 h. The solution was then neutralized to pH = 7 using 0.1 mol/L sodium hydroxide solution. For the experimental group, the neutralized solution was diluted to 100 mL in a volumetric flask. An aliquot of 30 mL of the diluted solution was transferred to a conical flask and titrated with 0.01 mol/L sodium hydroxide solution using bromothymol blue as the pH indicator. The volume of NaOH consumed was recorded as V_1. For the blank group, 30 mL of deionized water was titrated under the same conditions with 0.01 mol/L sodium hydroxide solution using bromothymol blue as the indicator, and the volume of NaOH consumed was recorded as V_2. The titration experiment was repeated three times, and the results were statistically analyzed and expressed as mean ± standard deviation. The imidazole ring content was calculated using Eq. 2,

$$W = \frac{2c(V_1 - V_2)\times 10^{-3}}{m} \times 100\% \quad (2)$$

where W (wt%) represents the imidazole ring content; c is the concentration of the sodium hydroxide solution; V_1 and V_2 (mL) are the volumes of NaOH solution consumed during titration for the experimental and blank groups, respectively; and m (g) is the mass of the sample.

RESULTS AND DISCUSSION

Microscopic Morphology of His-RCNs

The microscopic morphology of RCNs and His-RCNs was characterized by SEM. As shown in Fig. 1a and 1b, RCNs was found to exhibit a spherical morphology with uniform particle size. To further quantify the particle size distribution, 100 particles were randomly selected from the RCNs sample for analysis. The results (Fig. 1c) show that the average particle size of the prepared RCNs was 88.8 ± 2.1 nm. These results confirm the successful preparation of RCNs, providing a suitable matrix for the subsequent fabrication of His-RCNs.

Figures 1d, 1e, 1f, and 1g show the microscopic morphology of His-RCNs and its magnified image, indicating that His-RCNs still retains a spherical nanostructure. The particle size distribution of His-RCNs is presented in Fig. 1h, showing an average particle size of 39.3 ± 1.1 nm. Compared with RCNs, His-RCNs exhibited a smaller particle size, which may be attributed to the disruption of the original hydrogen-bonding network caused by $NaIO_4$ oxidation and His grafting, resulting in a reduction in the size of the cellulose nanospheres. The SEM results further confirm that the prepared His-RCNs had a spherical nanostructure.

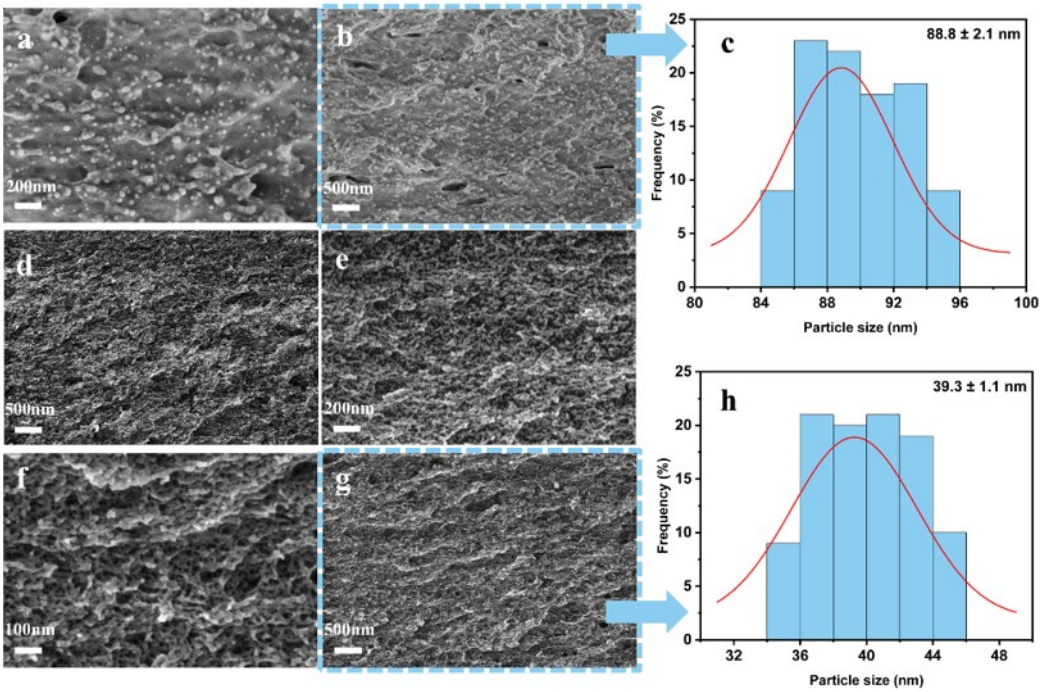

Fig. 1. (a) and (b) SEM images of RCNs; (d), (e), (f), and (g) SEM images of His-RCNs; (c) and (h) particle size distribution of RCNs and His-RCNs, respectively

Formation Process of His-RCNs

Figure 2 shows the FTIR spectra of raw cellulose, RCNs, DA-RCNs, His, and His-RCNs. As shown in Fig. 2a, the FTIR spectrum of raw cellulose exhibited typical cellulose absorption bands, with characteristic peaks appearing at 3448, 2891, 1644, 1432, 1372, 1058, and 893 cm^{-1}.

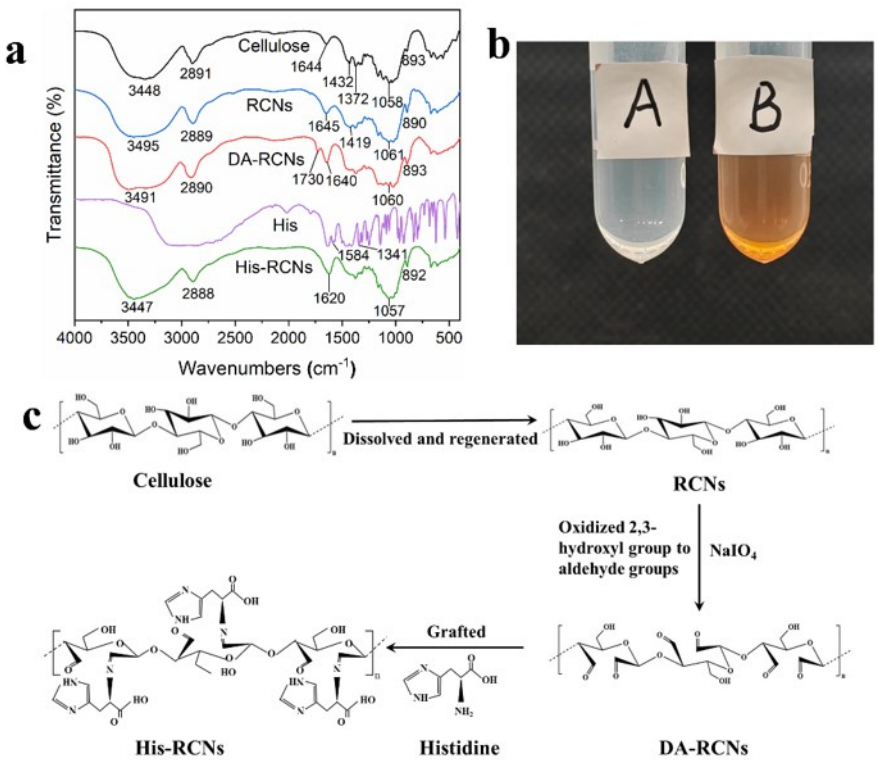

Fig. 2. (a) FTIR spectra of raw cellulose, RCNs, DA-RCNs, His, and His-RCNs; (b) Pauly color reaction of His; (c) Preparation process of His-RCNs

These peaks corresponded to the O–H stretching vibration of hydroxyl groups in cellulose (Alemdar and Sain 2008), C–H stretching vibration of –CH and –CH_2 groups (Yang *et al.* 2007), O–H bending vibration of adsorbed water (Plappert *et al.* 2018), O–H bending vibration of cellulose, C–H bending vibration (Arif *et al.* 2025), C–O stretching vibration of primary and secondary hydroxyl groups in cellulose (Huang *et al.* 2017), and the stretching vibration of β-1,4-glycosidic bonds (Plappert *et al.* 2018), respectively.

As shown in Fig. 2a, the FTIR spectrum of RCNs prepared *via* dissolution and regeneration exhibited an absorbance pattern similar to that of the raw cellulose, indicating that no chemical structural change occurred during the dissolution–regeneration process. However, the O–H bending vibration band of RCNs shifted from 1432 cm^{-1} to 1419 cm^{-1}, suggesting that the CH_2–OH group at the C6 position transforms from the tg conformation to the gt conformation after dissolution and regeneration. This shift confirmed the transition from cellulose I to cellulose II (Zhang *et al.* 2009). The FTIR characteristics of RCNs were consistent with those reported in previous studies (Zhang *et al.* 2024), further confirming the successful preparation of RCNs.

To obtain DA-RCNs, RCNs were oxidized with $NaIO_4$. Figure 2c illustrates the oxidation process, in which $NaIO_4$ cleaves the C2–C3 bond of the glucose units in cellulose, leading to the opening of the pyranose ring. During this reaction, the two secondary hydroxyl groups at the C2 and C3 positions were simultaneously converted into aldehyde groups (–CHO), resulting in nanocellulose with a dialdehyde structure. The FTIR spectrum of DA-RCNs was similar to that of RCNs, suggesting that the cellulose skeleton remained intact after $NaIO_4$ oxidation. However, the absorption band at 1060 cm^{-1} in the FTIR spectrum of DA-RCNs exhibited a noticeably reduced intensity compared with RCNs, reflecting a decrease in hydroxyl group content. In addition, a new absorbance peak

appeared at 1730 cm^{-1}, corresponding to the C=O stretching vibration of aldehyde groups (Mou 2017). These results confirmed that the hydroxyl groups of RCNs were oxidized into aldehyde groups by $NaIO_4$, indicating the successful preparation of dialdehyde cellulose.

In the FTIR spectrum of His, a broad band in the range of 3300 to 2500 cm^{-1} was attributed to the N–H and C–H stretching vibrations of the imidazole ring and carbon framework, together with the O–H stretching vibration of carboxylic acid dimers (Martin Britto Dhas *et al.* 2008; Moura *et al.* 2024). The peak at 1584 cm^{-1} corresponded to the stretching vibration of double bonds in the imidazole ring (Fawzy *et al.* 2018). Moreover, the band near 1341 cm^{-1} was assigned to complex ring vibrations of the imidazole ring, involving mixed modes, such as C–N and C–C stretching, as well as in-plane C–H bending (Vinayagamoorthy 2017). His-RCNs were obtained through a Schiff base reaction between DA-RCNs and His. Specifically, the reactive aldehyde groups (–CHO) on the DA-RCNs skeleton underwent a nucleophilic addition–elimination reaction with the primary amino groups ($–NH_2$) in the His structure, forming stable imine bonds (C=N–) and thereby covalently anchoring His molecules onto the surface of the cellulose nanospheres. In the FTIR spectrum of His-RCNs, the absorbance band at 1730 cm^{-1}, assigned to the stretching vibration of –CHO, disappeared, while a new band appeared at 1620 cm^{-1}, corresponding to the C=N stretching vibration, confirming that the aldehyde groups of DA-RCNs successfully condensed with the amino groups of His (Streater *et al.* 2024). Moreover, the characteristic peaks of cellulose at 3447, 2888, 1640, and 892 cm^{-1} remained present, indicating that the cellulose skeleton was preserved in the His-grafted dialdehyde nanocellulose composite. In addition, the imidazole ring content was determined by an acid–base titration method, and the mass fraction of imidazole rings was calculated to be 19.01 ± 0.37 wt%.

The successful preparation of His-RCNs was further verified by the Pauly color reaction (Ma *et al.* 2023). The Pauly reaction is a specific colorimetric reaction based on the imidazole group, in which the imidazole ring of His couples with diazotized sulfanilic acid (Pauly reagent) under alkaline conditions, forming orange-red to brown-red azo coupling products. In the test, an appropriate amount of the sample suspension was placed in a test tube, followed by the addition of a sulfanilic acid in dilute hydrochloric acid. Under an ice bath, a sodium nitrite solution was added dropwise, and the mixture was kept at a constant temperature to complete the diazotization reaction. Subsequently, a weak alkaline solution was slowly added to adjust the system to weak alkaline conditions, and the color change of the solution was recorded. Before the reaction, the suspension was colorless and transparent (Fig. 2b A), whereas after the reaction, the suspension turned noticeably brown (Fig. 2b B). This result confirmed that His was successfully grafted onto His-RCNs, which is consistent with the FTIR analysis.

Thermal Stability of His-RCNs

The thermal stability of His-RCNs was investigated by TG analysis (Fig. 3). Figures 3a and 3b present the TG curves and derivative thermogravimetry (DTG) curves of RCNs, His, and His-RCNs, respectively. For RCNs, a weight loss of less than 10 wt% occurred below 100 °C, which was attributed to the evaporation of absorbed moisture in the sample (Zhang *et al.* 2024). Subsequently, RCNs began to decompose at around 260 °C, and the maximum degradation rate was observed at approximately 347 °C. This behavior was associated with the disruption of the complex hydrogen-bonding network of RCNs and the thermal degradation of hydroxyl groups in cellulose. The degradation rate gradually decreased after 380 °C, where the remaining carbonaceous structures underwent further

degradation and rearrangement. The residual carbon content of RCNs at 800 °C was approximately 19%. For His, rapid degradation occurred in the range of 260 to 300 °C, corresponding to intramolecular dehydration of His. Further rapid degradation was observed between 300 and 380 °C, indicating that decarboxylation reactions of His occurred during this stage (Vraneš *et al.* 2021). In the temperature range of 400 to 800 °C, His degraded gradually, which was associated with the ring-opening oxidation of the imidazole ring and the structural rearrangement of the resulting char (Weiss *et al.* 2018). The residual carbon content at 800 °C was approximately 43%.

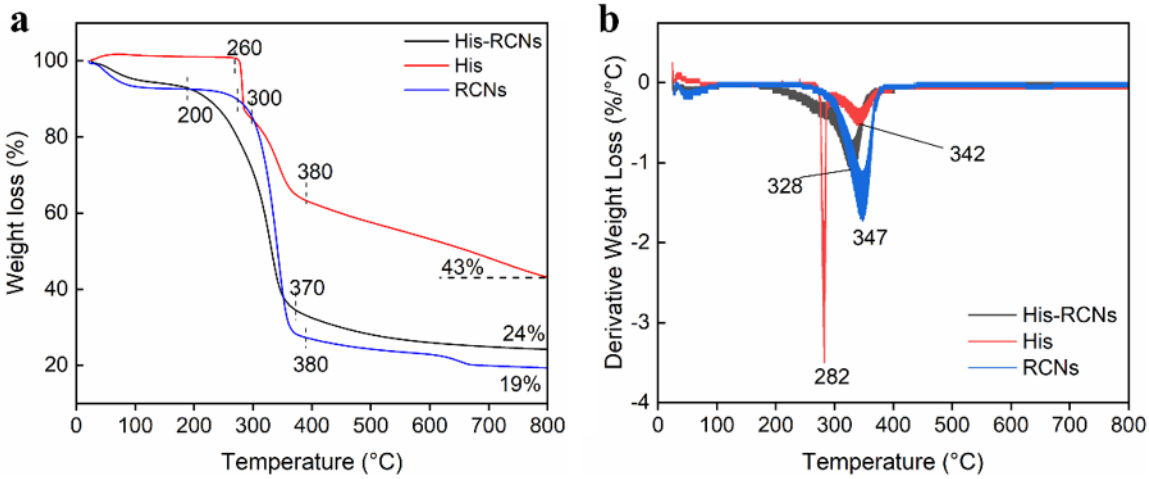

Fig. 3. (a) TG curves of His, RCNs, and His-RCNs; (b) DTG curves of His, RCNs, and His-RCNs

Notably, compared with RCNs, the initial degradation temperature of His-RCNs decreased from 260 °C to approximately 200 °C. This reduction can be attributed to the combined effects of dialdehyde modification and histidine grafting, both of which may disrupt the original hydrogen-bonding interactions within the cellulose network and consequently decrease the thermal resistance of the modified nanospheres. Subsequently, His-RCNs exhibited rapid mass loss in the temperature range of 200 to 370 °C, which was mainly attributed to the degradation of unmodified hydroxyl groups and residual aldehyde groups, with a minor contribution from intramolecular dehydration of the grafted components. In the final stage, the sample degraded gradually, leaving a residual carbon content of approximately 24%, which was higher than that of RCNs. This result indicated that the chemical modification altered the degradation and rearrangement pathways of the cellulose carbon skeleton, leading to the formation of more thermally stable carbonaceous structures. The TG results confirmed that His was successfully grafted onto DA-RCNs. Based on the calculation, the mass fraction of RCNs in His-RCNs was 79.2%, while the grafted His accounted for 20.8%, which was close to the imidazole ring content determined by acid–base titration. This further confirmed the successful grafting modification.

CONCLUSIONS

1. Starting from cellulose, RCNs with a nanosphere morphology and a particle size of 88.8 ± 2.1 nm were successfully prepared. The RCNs exhibited a chemical structure consistent with that of cellulose.

2. The RCNs were oxidized with $NaIO_4$ to obtain DA-RCNs, which were subsequently grafted with His to produce His-RCNs (particle size of 39.3 ± 1.1 nm). The morphology and structure of the prepared material were systematically characterized. Results from FTIR spectroscopy, SEM observation, and the Pauly color reaction confirmed that His was successfully grafted onto DA-RCNs *via* a Schiff base reaction. Meanwhile, the grafted product retained the fundamental cellulose skeleton and the spherical nanostructure of the nanocellulose particles.
3. Thermogravimetric analysis further indicated that the His-grafted spherical nanocellulose exhibited great thermal stability. Quantitative analysis revealed that the mass fraction of RCNs in the grafted product was 79.2%, while the grafted His accounted for 20.8%.
4. Due to the presence of the imidazole ring in histidine, which provides pH responsiveness, hydrogen-bonding capability, metal coordination ability, and π–π stacking interactions, the prepared His-RCNs hold promising potential as multifunctional bio-based platforms for applications in adsorption, catalysis, functional coatings, and other advanced material systems. The accessible imidazole functionalities may enable specific molecular interactions and provide additional active sites compared with pristine cellulose materials, thereby expanding the functional utilization of lignocellulosic resources.

ACKNOWLEDGMENTS

The authors acknowledge the support of the Two-support Programs for Discipline Construction of Sichuan Agricultural University; Provincial Undergraduate Training Program on Innovation and Entrepreneurship (No.S202610626077); the Science and Technology Project of China Tobacco Sichuan Industrial Co., Ltd. (10202314BA510).

Conflict of Interest

The authors declare no conflict of interest.

Data Availability Statement

The data are available from the corresponding author upon reasonable request.

REFERENCES CITED

Alemdar, A., and Sain, M. (2008). "Isolation and characterization of nanofibers from agricultural residues – Wheat straw and soy hulls," *Bioresource Technology* 99(6), 1664-1671. https://doi.org/10.1016/j.biortech.2007.04.029

Anderson, K. D., Marczewski, K., Singamaneni, S., Slocik, J. M., Jakubiak, R., Naik, R. R., Bunning, T. J., and Tsukruk, V. V. (2010). "Plasma amino acid coatings for a conformal growth of titania nanoparticles," *ACS Applied Materials & Interfaces* 2(8), 2269-2281. https://doi.org/10.1021/am1003365

Arif, S., Maan, A. A., Aadil, R. M., and Khan, M. K. I. (2025). "Assessing canola residue: A comprehensive analysis of composition, cellulose extraction and

characterization," *Cellulose* 32(14), 8185-8200. https://doi.org/10.1007/s10570-025-06736-z

Barazzouk, S., and Daneault, C. (2011). "Spectroscopic characterization of oxidized nanocellulose grafted with fluorescent amino acids," *Cellulose* 18, 643-653. http://doi.org/10.1007/s10570-011-9503-5

Chen, Y., Tao, K., Ji, W., Kumar, V. B., Rencus-Lazar, S., and Gazit, E. (2022). "Histidine as a key modulator of molecular self-assembly: Peptide-based supramolecular materials inspired by biological systems," *Materials Today* 60, 106-127. https://doi.org/10.1016/j.mattod.2022.08.011

Chung, W.-J., Oh, J.-W., Kwak, K., Lee, B. Y., Meyer, J., Wang, E., Hexemer, A., and Lee, S.-W. (2011). "Biomimetic self-templating supramolecular structures," *Nature* 478(7369), 364-368. https://doi.org/10.1038/nature10513

Cui, S., Wei, P., and Li, L. (2018). "Preparation of poly (propylene carbonate)/graphite nanoplates-spherical nanocrystal cellulose composite with improved glass transition temperature and electrical conductivity," *Composites Science and Technology* 168, 63-73. https://doi.org/10.1016/j.compscitech.2018.09.012

Das, R., Lindström, T., Sharma, P. R., Chi, K., and Hsiao, B. S. (2022). "Nanocellulose for sustainable water purification," *Chemical Reviews* 122(9), 8936-9031. https://doi.org/10.1021/acs.chemrev.1c00683

Dehghani, A., Bahlakeh, G., Ramezanzadeh, B., and Mofidabadi, A. H. J. (2021). "Improvement of the anti-corrosion ability of a silane film with β-cyclodextrin-based nanocontainer loaded with L-histidine: Coupled experimental and simulations studies," *Progress in Organic Coatings* 157, article 106288. https://doi.org/10.1016/j.porgcoat.2021.106288

Fawzy, A., Abdallah, M., Zaafarany, I. A., Ahmed, S. A., and Althagafi, I. I. (2018). "Thermodynamic, kinetic and mechanistic approach to the corrosion inhibition of carbon steel by new synthesized amino acids-based surfactants as green inhibitors in neutral and alkaline aqueous media," *Journal of Molecular Liquids* 265, 276-291. https://doi.org/10.1016/j.molliq.2018.05.140

Hsu, H. C., Tsao, J. C., Yeh, C. H., Wu, H. T., Wu, C. T., Wu, S. H., and Shih, C. F. (2024). "Large-area perovskite solar module produced by introducing self-assembled L-histidine monolayer at TiO_2 and perovskite interface," *Nanomaterials* 14(15), article 1315. https://doi.org/10.3390/nano14151315

Huang, J., Zhang, S., Zhang, F., Guo, Z., Jin, L., Pan, Y., Wang, Y., and Guo, T. (2017). "Enhancement of lignocellulose-carbon nanotubes composites by lignocellulose grafting," *Carbohydrate Polymers* 160, 115-122. https://doi.org/10.1016/j.carbpol.2016.12.053

Jia, Y., Qiu, T., Guo, L., Ye, J., He, L., and Li, X. (2020). "Preparation of pH responsive smart nanocontainer *via* inclusion of inhibitor in graphene/halloysite nanotubes and its application in intelligent anticorrosion protection," *Applied Surface Science* 504, article 144496. https://doi.org/10.1016/j.apsusc.2019.144496

Kim, M., Oh, J.W., Jeong, D.W., Cho, B., Chang, J., Shi, X., and Han, S.O. (2024). "Biosynthesis of l-histidine from marine biomass-derived galactans in metabolically engineered *Corynebacterium glutamicum*," *Bioresource Technology* 391, article 129963. https://doi.org/10.1016/j.biortech.2023.129963

Kovaleva, T. A., Holyavka, M. G., Rezvan, S. G., and Kozhedub, S. V. (2008). "Evaluation of the number of ionogenic groups of inulinase by acid-base titration,"

Bulletin of Experimental Biology and Medicine 145(6), 769-771. https://doi.org/10.1007/s10517-008-0183-6

Levin, A., Hakala, T. A., Schnaider, L., Bernardes, G. J. L., Gazit, E., and Knowles, T. P. J. (2020). "Biomimetic peptide self-assembly for functional materials," *Nature Reviews Chemistry* 4(11), 615-634. https://doi.org/10.1038/s41570-020-0215-y

Li, F., Mascheroni, E., and Piergiovanni, L. (2015). "The potential of nanocellulose in the packaging field: A review," *Packaging Technology and Science* 28(6), 475-508. https://doi.org/10.1002/pts.2121

Li, T., Chen, C., Brozena, A. H., Zhu, J. Y., Xu, L., Driemeier, C., Dai, J., Rojas, O. J., Isogai, A., Wågberg, L., *et al.* (2021). "Developing fibrillated cellulose as a sustainable technological material," *Nature* 590(7844), 47-56. https://doi.org/10.1038/s41586-020-03167-7

Li, N., Liu, T., Shi, C., Shi, X., Qian, H., Cao, Q., Chen, J., Huang, Y., Yu, X., and Jiang, B. (2025). "Biobased solvent-free fluids based on spherical cellulose nanocrystals for epoxy nanocomposite adhesive reinforcement," *Composites Science and Technology* 261, article 111007. https://doi.org/10.1016/j.compscitech.2024.111007

Lu, F., Yu, H., Yan, C., and Yao, J. (2016). "Polylactic acid nanocomposite films with spherical nanocelluloses as efficient nucleation agents: Effects on crystallization, mechanical and thermal properties," *RSC Advances* 6, 46008-46018. https://doi.org/10.1039/C6RA02768G

Ma, J. X., Liu, P., Wang, Y. X., Ren, X., Zhang, R., and Li, L. W. (2023). "A histidine-rich fusion tag enables real-time monitoring of recombinant protein expression by Pauly reaction-based colorimetric assay," *Biochemical and Biophysical Research Communications* 666, 128-136. https://doi.org/10.1016/j.bbrc.2023.05.004

Martin Britto Dhas, S. A., Bhagavannarayana, G., and Natarajan, S. (2008). "Growth and characterization of a new potential NLO material from the amino acid family—l-prolinium picrate," *Journal of Crystal Growth* 310(15), 3535-3539. https://doi.org/10.1016/j.jcrysgro.2008.04.049

Meena, M., Saharan, V., Meena, K. K., Singh, B., Pilania, S., Gupta, N. K., Pal, A., Garhwal, O. P., Sharma, Y. K., Singh, U., *et al.* (2024). "Synthesis and characterization of novel histidine functionalized chitosan nanoformulations and its bioactivity in tomato plant," *Scientific Reports* 14(1), article 15118. https://doi.org/10.1038/s41598-024-64268-1

Mhlongo, J. T., Nuapia, Y., Motsa, M. M., Mahlangu, T. O., and Etale, A. (2022). "Green chemistry approaches for extraction of cellulose nanofibers (CNFs): A comparison of mineral and organic acids," *Materials Today: Proceedings* 62, S57-S62. https://doi.org/10.1016/j.matpr.2022.02.088

Moon, R. J., Martini, A., Nairn, J., Simonsen, J., and Youngblood, J. (2011). "Cellulose nanomaterials review: Structure, properties and nanocomposites," *Chemical Society Reviews* 40(7), 3941-3994. https://doi.org/10.1039/C0CS00108B

Mou, K., Li, J., Wang, Y., Cha, R., and Jiang, X. (2017). "2,3-Dialdehyde nanofibrillated cellulose as a potential material for the treatment of MRSA infection," *Journal of Materials Chemistry B* 5(38), 7876-7884. https://doi.org/10.1039/C7TB01857F

Moura, M. J. d. S., Vasques, R. B., Magalhães, S. J. d. m., Almeida Neto, F. W. d. Q., de Lima Neto, P., dos Santos, L. P. M., Florez, M. A. C., Ribas, G. F., Medeiros, S. L. S., Salomão, F. C. C. S., *et al.* (2024). "Assessment of the amino acid L-histidine as a corrosion inhibitor for a 1018 carbon steel in aqueous sodium chloride solution," *Crystals* 14(8), article 703. https://doi.org/10.3390/cryst14080703

Österberg, M., Henn, K. A., Farooq, M., and Valle-Delgado, J. J. (2023). "Biobased nanomaterials─The role of interfacial interactions for advanced materials," *Chemical Reviews* 123(5), 2200-2241. https://doi.org/10.1021/acs.chemrev.2c00492

Plappert, S. F., Quraishi, S., Pircher, N., Mikkonen, K. S., Veigel, S., Klinger, K. M., Potthast, A., Rosenau, T., and Liebner, F. W. (2018). "Transparent, flexible, and strong 2,3-dialdehyde cellulose films with high oxygen barrier properties," *Biomacromolecules* 19(7), 2969-2978. https://doi.org/10.1021/acs.biomac.8b00536

Pradhan, D., Jaiswal, A. K., and Jaiswal, S. (2022). "Emerging technologies for the production of nanocellulose from lignocellulosic biomass," *Carbohydrate Polymers* 285, article 119258. https://doi.org/10.1016/j.carbpol.2022.119258

Ram, B., Chauhan, G. S., Mehta, A., Gupta, R., and Chauhan, K. (2018). "Spherical nanocellulose-based highly efficient and rapid multifunctional naked-eye Cr(VI) ion chemosensor and adsorbent with mild antimicrobial properties," *Chemical Engineering Journal* 349, 146-155. https://doi.org/10.1016/j.cej.2018.05.085

Rampazzo, R., Alkan, D., Gazzotti, S., Ortenzi, M. A., Piva, G., and Piergiovanni, L. (2017). "Cellulose nanocrystals from lignocellulosic raw materials, for oxygen barrier coatings on food packaging films," *Packaging Technology and Science* 30(10), 645-661. https://doi.org/10.1002/pts.2308

Rani, M., Singh, G., Siddiqi, R.A., Gill, B.S., Sogi, D.S., and Bhat, M.A. (2021). "Comparative quality evaluation of physicochemical, technological, and protein profiling of wheat, rye, and barley cereals," *Frontiers in Nutrition* 8. https://doi.org/10.3389/fnut.2021.694679

Shojaeiarani, J., Bajwa, D. S., and Chanda, S. (2021). "Cellulose nanocrystal based composites: A review," *Composites Part C: Open Access* 5, article 100164. https://doi.org/10.1016/j.jcomc.2021.100164

Streater, D. H., Kennehan, E. R., Wang, D., Fiankor, C., Chen, L., Yang, C., Li, B., Liu, D., Ibrahim, F., Hermans, I., *et al.* (2024). "Control over charge separation by imine structural isomerization in covalent organic frameworks with implications on CO_2 photoreduction," *Journal of the American Chemical Society* 146(7), 4489-4499. https://doi.org/10.1021/jacs.3c10627

Sun, B., Hou, Q., Liu, Z., and Ni, Y. (2015). "Sodium periodate oxidation of cellulose nanocrystal and its application as a paper wet strength additive," *Cellulose* 22(2), 1135-1146. https://doi.org/10.1007/s10570-015-0575-5

Tian, L., Qi, L., Liu, Y., Zhao, Z., and Liu, W. (2024). "Boosting the LAC-like activity of tetrapeptide capped copper nanoparticle-based nanozymes for colorimetric determination of adrenaline," *Analytical Methods* 16(9), 1383-1389. https://doi.org/10.1039/D3AY02328A

Tian, W., Gao, X., Zhang, J., Yu, J., and Zhang, J. (2022). "Cellulose nanosphere: Preparation and applications of the novel nanocellulose," *Carbohydrate Polymers* 277, article 118863. https://doi.org/10.1016/j.carbpol.2021.118863

Vinayagamoorthy, R., Irudayaraj, A. A., Raj, A. D., Karthick, S., and Jayakumar, G. (2017). "Comparative study of properties of L-histidine and L-histidine nickel nitrate hexahydrate crystals grown by slow evaporation," *Mechanics, Materials Science & Engineering Journal* 9, 1-7. https://doi.org/10.2412/mmse.83.74.689

Vraneš, M., Panić, J., Tot, A., Papović, S., Gadžurić, S., Podlipnik, Č., and Bešter-Rogač, M. (2021). "From amino acids to dipeptide: The changes in thermal stability and hydration properties of β-alanine, L-histidine and L-carnosine," *Journal of Molecular Liquids* 328, article 115250. https://doi.org/10.1016/j.molliq.2020.115250

Weiss, I. M., Muth, C., Drumm, R., and Kirchner, H. O. K. (2018). "Thermal decomposition of the amino acids glycine, cysteine, aspartic acid, asparagine, glutamic acid, glutamine, arginine and histidine," *BMC Biophysics* 11(1), article 2. https://doi.org/10.1186/s13628-018-0042-4

Yang, C. J., Nguyen, D. D., and Lai, J. Y. (2023). "Poly(l-histidine)-mediated on-dem- and therapeutic delivery of roughened ceria nanocages for treatment of chemical eye injury," *Advanced Science* 10(26), article 2302174. https://doi.org/10.1002/advs.202302174

Yang, H., Yan, R., Chen, H., Lee, D. H., and Zheng, C. (2007). "Characteristics of hemicellulose, cellulose and lignin pyrolysis," *Fuel* 86(12-13), 1781-1788. https://doi.org/10.1016/j.fuel.2006.12.013

Yuan, H., Zhao, Z., Wang, C., Gao, H., and Nie, Y. (2025). "Functional nanocellulose hydrogel with amino acid integration for enhanced Li/Fe separation in $LiFePO_4$ batteries," *International Journal of Biological Macromolecules* 298, article 140018. https://doi.org/10.1016/j.ijbiomac.2025.140018

Yupanqui-Mendoza, S. L., and Arantes, V. (2024). "Recent advances in cellulose nanospheres: Production, formation mechanisms, properties and applications," *Cellulose* 31(18), 10609-10649. https://doi.org/10.1007/s10570-024-06229-5

Zhang, S., Fu, C. F., Li, F., Yu, J., and Gu, L. (2009). "Direct preparation of a novel membrane from unsubstituted cellulose in NaOH complex solution," *Iranian Polymer Journal* 18(10), 767-776.

Zhang, L., Sheng, Y., Zehtab Yazdi, A., Sarikhani, K., Wang, F., Jiang, Y., Liu, J., Zheng, T., Wang, W., Ouyang, P., *et al.* (2019). "Surface-assisted assembly of a histidine-rich lipidated peptide for simultaneous exfoliation of graphite and functionalization of graphene nanosheets," *Nanoscale* 11(6), 2999-3012. https://doi.org/10.1039/C8NR08397E

Zhang, S., Zhu, G., Xu, X., Luo, F., Tian, D., Liu, Y., Wang, Q., Chen, Q., Jiang, Y., Qi, J., *et al.* (2024). "Two all-biomass cellulose/amino acid spherical nanoadsorbents based on a tri-aldehyde spherical nanocellulose II amino acid premodification platform for the efficient removal of Cr(VI) and Cu(II)," *International Journal of Biological Macromolecules* 258, article 128748. https://doi.org/10.1016/j.ijbiomac.2023.128748

Zheng, D., Deng, Y., Xia, Y., Nan, Y., Peng, M., Wang, X., and Yue, J. (2019). "Fabrication and performance of a spherical cellulose nanocrystal-based hydrophobic drug delivery vehicle using rubber wood," *BioResources* 14(4), 7763-7774. https://doi.org/10.15376/biores.14.4.7763-7774

Article submitted: March 14, 2026; Peer review completed: July 4, 2026; Revised version received: July 13, 2026; Accepted: August 3, 2026; Published: August 14, 2026.
DOI: 10.15376/biores.21.4.9747-9760